Electronic Supplementary Information (ESI)

Toward efficient electrocatalytic oxygen evolution with a low concentration baking soda activated IrO_x surface in a hydrothermal medium

Yuling Hu[a,†], Chenglong Ma[b,†], Gan Du[a], Hanqing Gao[a], Xinlong Tian[c], Huamei Yu[a,], Jianjun Liao[a], Chengjun Ge[a], Ji Yang[b], Wei Sun[a,*]*

a. Key Laboratory of Agro-Forestry Environmental Processes and Ecological Regulation of Hainan Province, College of Ecology and Environment, Hainan University, 58 Renmin Road, Haikou 570228, P.R. China.

b. State Environmental Protection Key Laboratory of Environmental Risk Assessment and Control on Chemical Processes, School of Resources and Environmental Engineering, East China University of Science and Technology, 130 Meilong Road, Shanghai 200237, P.R. China.

c. State Key Laboratory of Marine Resource Utilization in South China Sea, Hainan University, 58 Renmin Road, Haikou 570228, P.R. China.

KEYWORDS. Iridium oxides, oxygen evolution reaction, baking soda, edge-shared, green synthesis.

*Corresponding author

Email address: weisun@hainanu.edu.cn

EXPERIMENTAL METHODS

Section-1: Materials preparation

All chemicals and solvents used in the experiments were of analytical grade and used without additional purification. Baking soda (BS), Sodium carbonate (BC), Sodium hydroxide (SH), Potassium bicarbonate (PB), Potassium carbonate (PC), Potassium hydroxide (PH) and sulfuric acid (H_2SO_4) were purchased from Macklin Co. Ltd., China. The iridium (IV) chloride ($H_2IrCl_6 \cdot 6H_2O$) was purchased from TCI Co. Ltd. (Shanghai). Deionized water (18.4 MΩ cm) was prepared in the laboratory to prepare the different solutions.

Crystalline and amorphous IrO_x: First, 5 g of $H_2IrCl_6 \cdot 6H_2O$ was completely dissolved in 250 mL of ultrapure water (concentration is 20 mg/L), and then take 4 mL of solution to added into 20 mL of the low concentration (0.05 M) of baking soda. Then, the mixture solution was transferred into a 40 mL Teflon-lined pressure vessel and heated in an oven at 150 °C for 12 h. The precipitates were suction-filtered and washed with deionized water twice to remove other ions. The remaining solid on the filter membrane was dried in an oven at 50 °C for at least 30 min. Finally, the obtained powders were calcined at temperature of 400 °C and maintained for 12 h. Here, the finally obtained IrO_x nanoparticles (NPs) was characterized by XRD, and be confirmed it belong to crystalline IrO_x NPs (we named it as SC-c-IrO_x). For preparing the amorphous IrO_x (we named it as BS-a-IrO_x), the pre-treatment processes (include hydrothermal and purification) are consistent with the SC-c-IrO_x, the difference is that the annealing temperature was set at 350°C and the duration is reduced to 6h. The synthesis of IrOx NPs under two other sodium bases (sodium carbonate and sodium hydroxide) media is identical to that of baking soda media. For the crystalline structure of IrO_x NPs, we named SC-c-IrO_x and SH-c-IrO_x, respectively; for the amorphous IrO_x NPs, we named SC-a-IrO_x and SH-a-IrO_x, respectively. It should be noted that the above named IrO_x NPs are only for media at 0.05 M concentration, and the method for synthesizing IrO_x NPs at higher media concentrations is essentially the same as at 0.05 M concentration.

The preparation of IrO_x NPs under three potassium bases (potassium bicarbonate-PB, potassium carbonate-PC, potassium hydroxide-PH) is consistent with that of sodium bases. After pre-treatment processes, the obtained IrO_x powders were calcined temperature of 400 °C and maintained for 12 h.

Section-2: Electrode preparation and Electrochemical Measurements

The electrodes used for the electrochemical measurements were prepared similar to traditional dimensional stable anode (DSA). First, 5 mg of fresh catalyst powders as dispersed into a solution mixed with 1.5 mL of 2:1 (v/v) isopropanol/water. Then the solution was ultrasonicated for approximately 30 min to achieve homogeneity. Next, 7.5 μL of the homogenized solution was deposited on a tailored Ti plate (0.5 cm × 1.5 cm), which was etched for 2 h by 10% (wt %) oxalic acid under near boiling condition. The deposition process was repeated 5 times to obtain a mass loading approximately 0.15 mg cm^{-2}. For each time, the electrodes of covered by BS-c-IrO_x, SC-c-IrO_x and SH-c-IrO_x catalyst was annealed in an oven at 400 ºC for 10 min, and the last time was

expanded to 60 min. But the electrodes of covered by BS-a-IrO_x, SC-a-IrO_x and SH-a-IrO_x catalyst was annealed at 350 ºC not the 400 ºC.

Electrochemical tests were performed in a three-electrode system. Here, an Ag/AgCl was employed as the reference, and a polished and cleaned Pt foil with a 1.5 cm × 1 cm reaction area was used as the counter electrode. All tests were carried out in 0.5M H_2SO_4 as electrolyte solution. The working electrodes were cycled at least 20 times at the potential windows of -0.2V-1.2V (vs. Ag/AgCl) until the curves overlapped in the cyclic voltammetry (CV) experiments; then the CV data and polarization curves were recorded at the specified electrochemical measurements. The activity with iR-compensation was detected by the linear scan voltammetry (LSV) method with a scan rate of 5 mV s^{-1}. The solution resistance is determined by the electrochemical impedance spectroscopy (EIS), which was conducted at 1.35 V vs. The electrode potential was converted from the Ag/AgCl scale to the Reversible Hydrogen Electrode (RHE) scale by a calibration equation: E (RHE) = E (Ag/AgCl) + 0.197V + 0.0592×pH − iR, where R is the uncompensated ohmic electrolyte resistance measured by the high-frequency AC impedance (10^6−0.1 Hz). According to the different electrodes Nyquist plots from the EIS spectra, the solution resistances and electrons transfer resistances were extracted by fitting the plot. Commonly, the conducted potential was set at 1.55V with an amplitude of 10 mV. The multi-current step was used to test the stability of the electrodes. Set a maximum voltage of 2 V (vs. Ag/AgCl) as a point of inactivation and the step current densities adjusting from 10 mA cm^{-2} to 50 mA cm^{-2} with each step maintain 10000s.

Section-3: Materials Characterization

The crystal structure of the catalysts was investigated by using powder X-ray diffraction (XRD), which equipped with a D/max2550 V apparatus and a Cu-Kα radiation source (λ=1.5406 Å), and the data were recorded from 10 to 80° at the step size of 0.02°. A JEM-2100 transmission electron microscope (TEM) was used to observe the surface morphology. UV-Vis spectra were conducted as below: firstly, the spectra of pure alkaline medium with a concentration of 0.05M and 20 mg/L $H_2IrCl_6{\cdot}6H_2O$ solution were measured. Then, adding 20 mg/L $H_2IrCl_6{\cdot}6H_2O$ to the selected BS, SC and SH three sodium alkali medium solution of 1:5 v/v. Determination of the ultraviolet spectrum of the mixed solution after 1h, 3h, 8h and 20h reaction time. The measurement method of NH_4HCO_3 solution as medium is the same as above.

The surface properties of the catalysts were determined via X-ray photoelectron spectroscopy (XPS) using an ESCALAB 250Xi instrument with Al-Kα radiation source at an energy step size of 0.05 eV. The samples were sputter-coated with carbon, thus, the XPS spectra were calibrated by C-*1s* at the binding energy of 284.8 eV. The X-ray absorption (XAS) data of the samples were recorded at room temperature in the Shanghai Synchrotron Radiation Facility (SSFR, beamline BL14W1, Shanghai) and National Synchrotron Radiation Laboratory (NSRL, beamline BL11U, Hefei), China.

Section 4: DFT calculation details

The Vienna Ab-initio Simulation Package (VASP) was adopted in this work using the projector augmented wave (PAW) method with the generalized gradient approximation

(GGA) for the exchange-correlation functional. A cutoff kinetic energy of 400 eV was set. The self-consistent field (SCF) was set to 1×10^{-5} eV/atom. The structure optimization force threshold was set to 0.02 eV/Å. The Brillouin zone integration was performed using a 5×5×3 Gamma k-point centered Monkhorst–Pack grids for the bulk structure of $Ir_8O_{16}H_8$. The 3×3×8 Monkhorst-Pack k-point setups were used for the 2×2 supercell bulk structure of $Ir_8O_{16}H_2$ constructed basing on the IrO_2 cell. The 3×2×1 Monkhorst–Pack k-point setups were used for 1×1 supercell structure optimization of the Ir-brookite surface. A 1×1 $Ir_8O_{16}H_8$ (210) with four layers, which serve as the slab. The Ir with unsaturated coordination was served as the adsorption site. Details for the calculation of IrO_2 could be found in our previous work[1]. For the free energy of the OER intermediates, the detailed computational method used has been widely described by Nørskov et al. The DOS was calculated by the Gaussian smearing method with a width of 0.1 eV.

The OER avtivities on the constructured slab model was further studies. Herein, the adsorbed oxygen mechanism (AEM) was considered in the acidic environment in this work. The following four electron transfer steps were considered,

(1) $*+H_2O\ (l) =*OH+H^++e^-$

(2) $*OH=*O\cdot+H^++e^-$

(3) $*O\cdot+H_2O=*OOH+H^++e^-$

(4) $*OOH =*+O_2\ (g)+H^++e^-$

Where * represent the adsord site on the slab model. H_2O (l) represent the liquid phase of water, O_2 (g) represent the gas phase of oxygen.

The adsorption energy of *OH，*O, and *OOH was calculate according to the following equation,

$$\Delta E_{(OH^*)}= E_{(slab\text{-}OH)}- E_{(slab)}-(E_{(H20)})-1/2E_{(H2)})$$

$$\Delta E_{(O^*)}= E_{(slab\text{-}O)}- E_{(slab)}-(E_{(H20)})-E_{(H2)})$$

$$\Delta E_{(OOH^*)}= E_{(slab\text{-}OOH)}- E_{(slab)}-(2E_{(H20)})-3/2E_{(H2)})$$

Where the $E_{(slab)}$ represent the calculate total energy of slab model, the $E_{(slab\text{-}OH)}$, $E_{(slab\text{-}O)}$, and $E_{(slab\text{-}OOH)}$ represent the total energy of slab model with the *OH, *O, and *OOH species respectively. $E_{(H20)}$ represent the energy of liquid phase of water, which equals the energy of gaseous water molecule at saturated vapor pressure at 298.15K. the $E_{(H2)}$ represent the energy of gas hydrogen molecule.

As for the each step, the adsorb free energy ΔG was calculate according to the following equation.

$$\Delta G= \Delta E-\Delta ZPE-T\Delta S+\Delta G_U$$

where ΔE is the adsorption energy above-mentioned. ΔZPE is the zero point energy which was calculated from sum of vibrational mode energies. TΔS was extracted from database of CRC handbook. ΔG_U equals -eU, U represent the potential applied on the materials. e is the charge transfer. The $G_{(O2)}$ was calculated according to the equation $2G(H_2O)-2G(H_2)-G(O_2)=-4.92$eV.

FIGURES AND TABLES

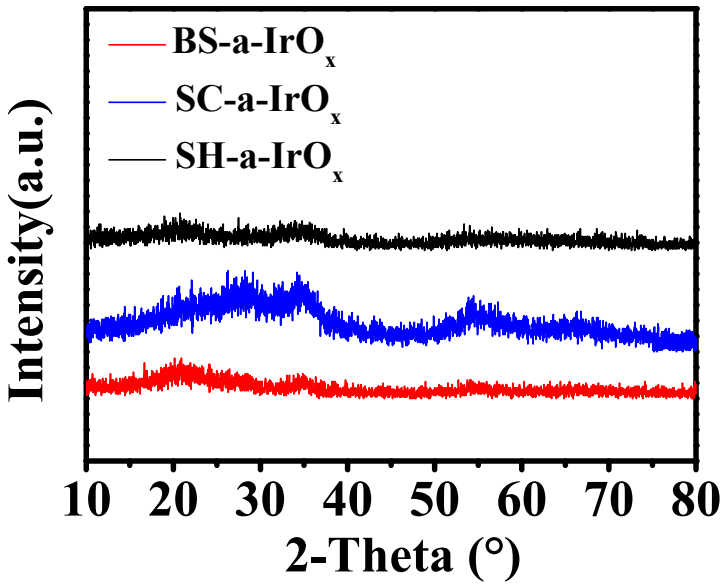

Figure S1. XRD patterns of prepared IrO_x NPs in selected three sodium bases. The IrO_x NPs are annealed at 350 for 6 h. There are no obvious diffraction peaks of IrO_2 (PDF-15-0870) as indicated by XRD, so we think they all are belong to amorphous.

Table S1. Summary of representative Ir-based electrocatalysts for OER.

Catalysts	Electrolyte	η (mV) at 10 mA cm^{-2}	Tafel slope mV dec^{-1}	Ref.
Ir-Pd NWs	0.5 M H_2SO_4	297	60	[1]
Commercial IrO_2	0.5 M H_2SO_4	320	76.3	[2]
Porous carbon-coated IrCo	0.5 M H_2SO_4	270	71.8	[2]
Rutile IrO_2	0.5 M H_2SO_4	435	68	[3]
Li-IrO_x	0.5 M H_2SO_4	290	39	[3]
IrO_2 NPs	0.5 M H_2SO_4	290	82	[4]
IrO_2/GCN	0.5 M H_2SO_4	276	57	[4]
IrO_x (20-30 nm)	0.5 M H_2SO_4	339	47	[5]
IrO_x-Mill	0.5 M H_2SO_4	442	85	[6]
Sr_2IrO_4	0.5 M H_2SO_4	287	45	[6]
Commercial Ir/C	0.5 M H_2SO_4	356	56	[7]
IrO_x-400°C	0.5 M H_2SO_4	295	77	[8]
Commercial IrO_2	0.5 M H_2SO_4	370	73	[8]
IrO_2@NC	0.5 M H_2SO_4	283	75.9	[9]
$Rh_{22}Ir_{78}$ alloy NPs	0.5 M H_2SO_4	292	101	[10]
TiN/IrO_2	0.5 M H_2SO_4	313	65.5	[11]
IrO_2/CNT	0.5 M H_2SO_4	293	67	[12]
SH-c-IrO_x	0.5 M H_2SO_4	366	75	This work
SC-c-IrO_x	0.5 M H_2SO_4	323	66	This work
BS-c-IrO_x	0.5 M H_2SO_4	303	61	This work
SH-a-IrO_x	0.5 M H_2SO_4	312	69	This work
SC-a-IrO_x	0.5 M H_2SO_4	310	68	This work
BS-a-IrO_x	0.5 M H_2SO_4	**295**	**53**	This work

References

[1] P. Lettenmeier, L. Wang, U. Golla-Schindler, P. Gazdzicki, N.A. Canas, M. Handl, R. Hiesgen, S.S. Hosseiny, A.S. Gago, K.A. Friedrich, Nanosized IrOx-Ir Catalyst with Relevant Activity for Anodes of Proton Exchange Membrane Electrolysis Produced by a Cost-Effective Procedure, Angew Chem Int Edit, 55 (2016) 742-746.

[2] X.C. Sun, F. Liu, X. Chen, C.C. Li, J. Yu, M. Pan, Iridium-doped ZIFs-derived porous carbon-coated IrCo alloy as competent bifunctional catalyst for overall water splitting in acid medium, Electrochim Acta, 307 (2019) 206-213.

[3] J.J. Gao, C.Q. Xu, S.F. Hung, W. Liu, W.Z. Cai, Z.P. Zeng, C.M. Jia, H.M. Chen, H. Xiao, J. Li, Y.Q. Huang, B. Liu, Breaking Long-Range Order in Iridium Oxide by Alkali Ion for Efficient Water Oxidation, J Am Chem Soc, 141 (2019) 3014-3023.

[4] J.Y. Chen, P.X. Cui, G.Q. Zhao, K. Rui, M.M. Lao, Y.P. Chen, X.S. Zheng, Y.Z. Jiang, H.G. Pan, S.X. Dou, W.P. Sun, Low-Coordinate Iridium Oxide Confined on Graphitic Carbon Nitride for Highly Efficient Oxygen Evolution, Angew Chem Int Edit, 58 (2019) 12540-12544.

[5] F. Song, X.L. Hu, Exfoliation of layered double hydroxides for enhanced oxygen evolution catalysis, Nat. Commun., 5 (2014).

[6] A.L. Strickler, D. Higgins, T.F. Jaramillo, Crystalline Strontium Iridate Particle Catalysts for

Enhanced Oxygen Evolution in Acid, Acs Appl Energ Mater, 2 (2019) 5490-5498.
[7] J.Y. Xu, Z. Lian, B. Wei, Y. Li, O. Bondarchuk, N. Zhang, Z.P. Yu, A. Araujo, I. Amorim, Z.C. Wang, B. Li, L.F. Liu, Strong Electronic Coupling between Ultrafine Iridium-Ruthenium Nanoclusters and Conductive, Acid-Stable Tellurium Nanoparticle Support for Efficient and Durable Oxygen Evolution in Acidic and Neutral Media, Acs Catal, 10 (2020) 3571-3579.
[8] B. Jiang, J. Kim, Y.N. Guo, K.C.W. Wu, S.M. Alshehri, T. Ahamad, N. Alhokbany, J. Henzie, Y. Yamachi, Efficient oxygen evolution on mesoporous IrOx nanosheets, Catal Sci Technol, 9 (2019) 3697-3702.
[9] S.Y. Hao, Y.H. Wang, G.K. Zheng, L.S. Qiu, N. Xu, Y. He, L.C. Lei, X.W. Zhang, Tuning electronic correlations of ultra-small IrO2 nanoparticles with La and Pt for enhanced oxygen evolution performance and long-durable stability in acidic media, Appl Catal B-Environ, 266 (2020).
[10] H.Y. Guo, Z.W. Fang, H. Li, D. Fernandez, G. Henkelman, S.M. Humphrey, G.H. Yu, Rational Design of Rhodium-Iridium Alloy Nanoparticles as Highly Active Catalysts for Acidic Oxygen Evolution, ACS Nano, 13 (2019) 13225-13234.
[11] K.K. Zhang, W.S. Mai, J. Li, H. Wang, G.Q. Li, W. Hu, Highly scattered Ir oxides on TiN as an efficient oxygen evolution reaction electrocatalyst in acidic media, J Mater Sci, 55 (2020) 3507-3520.
[12] J.Q. Guan, D. Li, R. Si, S. Miao, F.X. Zhang, C. Li, Synthesis and Demonstration of Subnanometric iridium Oxide as Highly Efficient and Robust Water Oxidation Catalyst, Acs Catal, 7 (2017) 5983-5986.

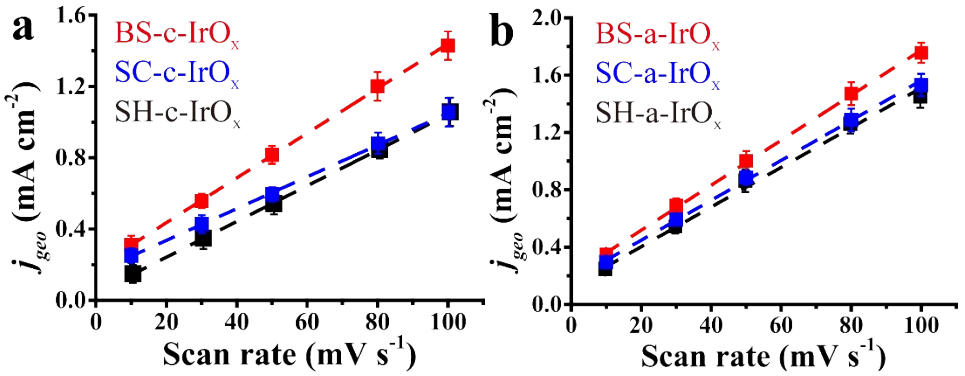

Amorphous IrO_x	BS-a-IrO_x	SC-a-IrO_x	SH-a-IrO_x
C_{dl} value (F cm^{-2})	0.0157	0.0141	0.0135

Crystalline IrO_x	BS-a-IrO_x	SC-a-IrO_x	SH-a-IrO_x
C_{dl} value (F cm^{-2})	0.0123	0.0095	0.0089

Figure S2. (a)-(b) The linear fitting of capacitive current with scan rate. To obtain the accurate C_{dl}, the current range is selected as the Faraday current-free region. All the materials show a good linearity, and the responding values of slope means that of C_{dl}, and their values are presented in the table below of figure. The all electrodes area is the same with a 0.25 cm^2 and electrolyte is the 0.5 M H_2SO_4.

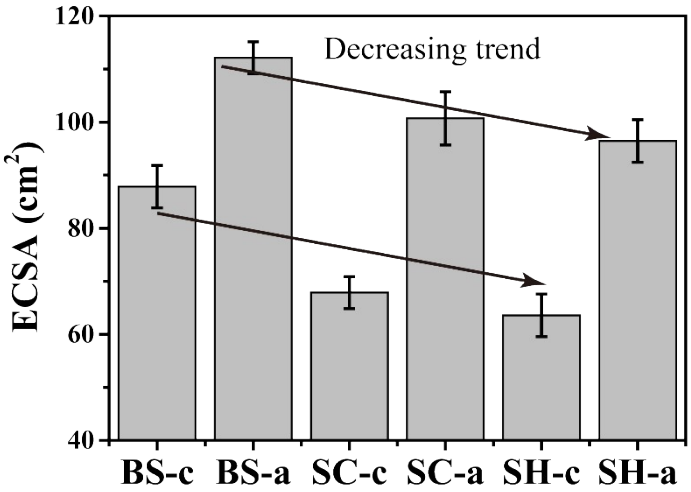

Figure S3. The calculated ECSAs of prepared different IrOx NPs. Based on the obtained of values of C_{dl}, the ECSAs were calculated by equation of ECSAs = C_d/C_s, where C_s=0.035 mF cm^{-2} based on the reported iridium-based materials value (*J. Am. Chem. Soc.* **2013,** *135* (45), 16977-16987). the ECSAs of IrOx NPs prepared under the three sodium-alkali follow the trend of that BS>SC>SH, and independent with the crystalline states (amorphous or crystalline).

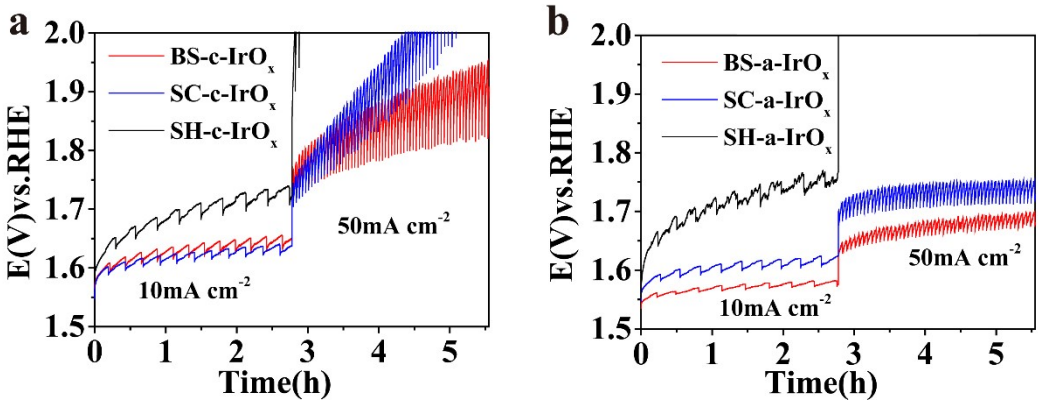

Figure S4. Evaluation of the OER stability of prepared different IrO_x NPs under the 0.5 M H_2SO4 electrolyte using chronopotentiometry (CP) at stepwise constant current. (a) for the crystalline IrO_x and (b) for the amorphous IrO_x. The first step corresponding to the 10 mA cm^{-2} and the second step is the 50 mA cm^{-2}, and there is a 2 s resting time between them. The mass loading on Ti plate was ~0.15 mg cm^{-2}, electrode area~0.2 cm^2, no Nafion was added.

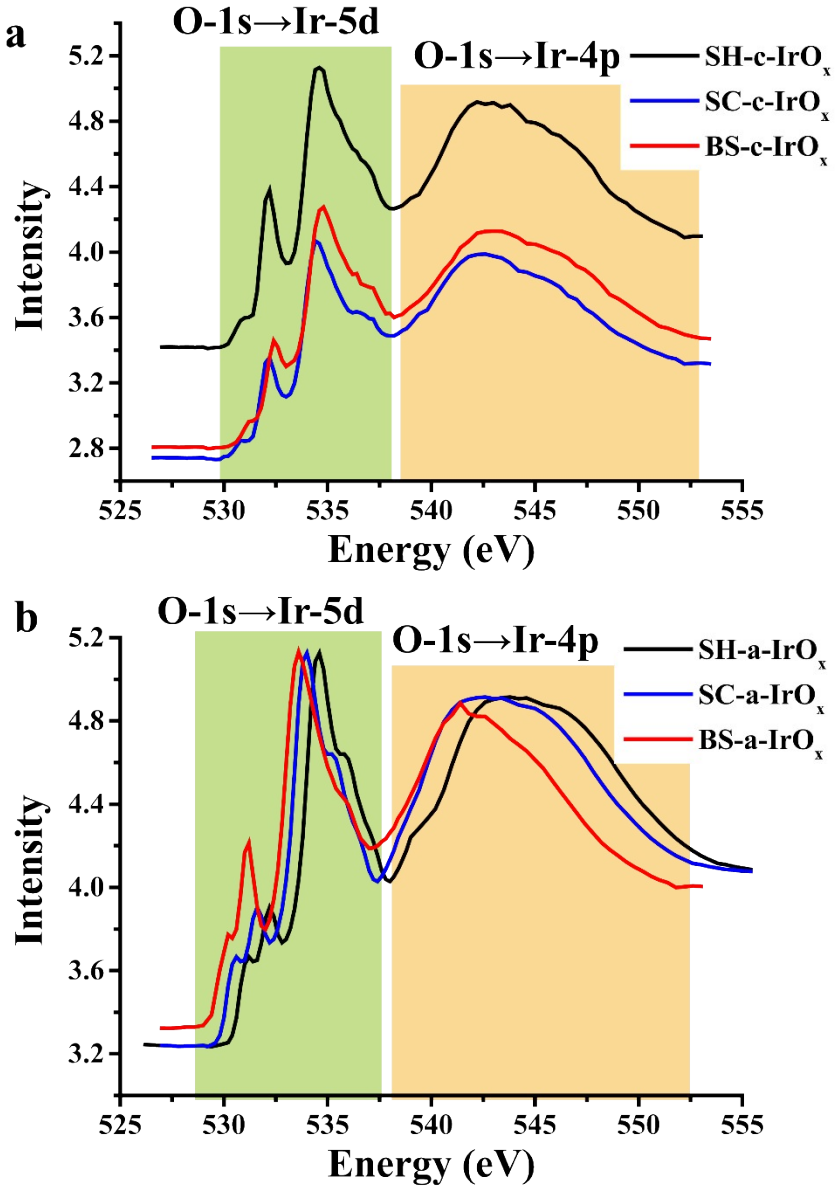

Figure S5. Full spectra of O-K XAS of prepared different IrO_x. The O-K XAS is consist of pre-edges from O-1s→Ir-5d and post peaks from O-1s→Ir-4p. (a) for the crystalline and (b) for the amorphous.

Table S2. The fitted results of O-K XAS of prepared different IrO_x NPs.

	J=3/2		**J=1/2**		**d_{xy}**		**d_{z2}**	
	E (eV)	Area[a]	E (eV)	Area	E (eV)	Area	E (eV)	Area
SH-c-IrO_x	530.85	1	532.21	5.8	534.49	13.7	536.25	10.3
SC-c-IrO_x	530.85	1	532.19	6.1	534.47	20.5	536.45	13.5
BS-c-IrO_x	531.22	1	532.47	5.6	534.66	17.5	536.62	11.2
SH-a-IrO_x	531.10	1	532.22	2.0	534.46	9.7	536.07	5.6
SC-a-IrO_x	530.48	1	531.59	2.3	533.86	9.6	535.46	7.7
BS-a-IrO_x	530.05	1	531.13	3.7	533.53	9.9	535.26	8.7

Notes: [a]- Since the peak with J=3/2 is the weakest, we use it as a benchmark and set the value to 1, while the other peaks area is multiples of J=3/2.

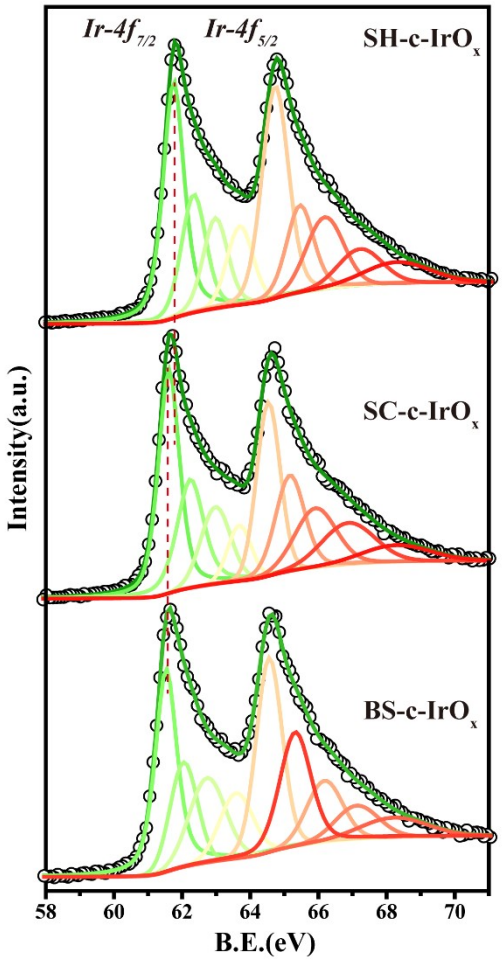

Catalysts	B.E. (eV) of Ir-4f$_{7/2}$
SH-c-IrO$_x$	61.75
SC-c-IrO$_x$	61.60
BS-c-IrO$_x$	61.55

Figure S6. The performed Ir-4f XPS spectra of crystalline IrO_x NPs. All the spectra are calibrated by C-1s at the binding energy of 284.8 eV. The binding energy of splitting peak of Ir-4f$_{7/2}$ is listed right. Many researches revealed that the B.E. of Ir-4f7/2 in IrO_2 located around 61.5~61.8 eV, but most of gives a value of 61.7 eV, thereby, the prepared SH-c-IrO_x is agreement with reports.

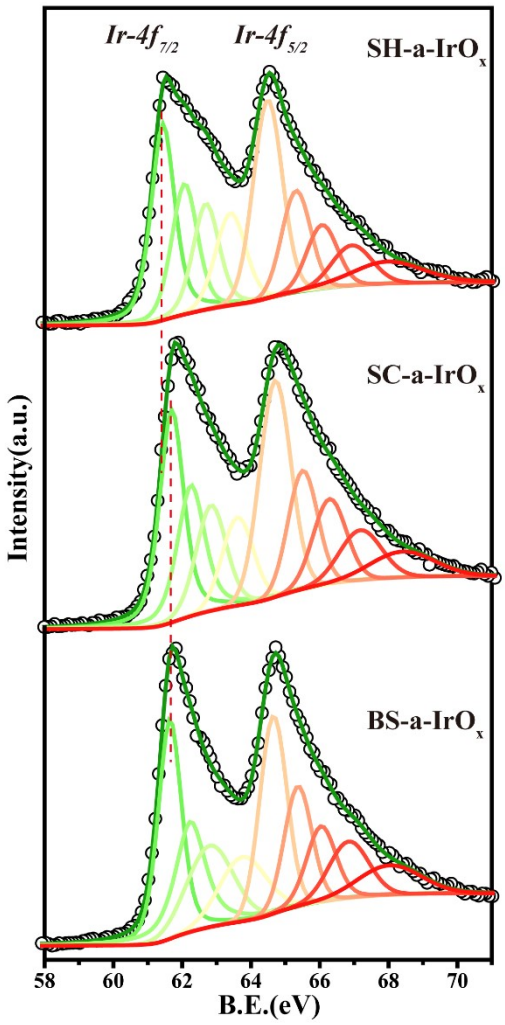

Catalysts	B.E. (eV) of Ir-4f$_{7/2}$
SH-a-IrO$_x$	61.45
SC-a-IrO$_x$	61.70
BS-a-IrO$_x$	61.65

Figure S7. The performed Ir-4f XPS spectra of amorphous IrO$_x$ NPs. All the spectra are calibrated by C-1s at the binding energy of 284.8 eV. The binding energy of splitting peak of Ir-4f$_{7/2}$ is listed right.

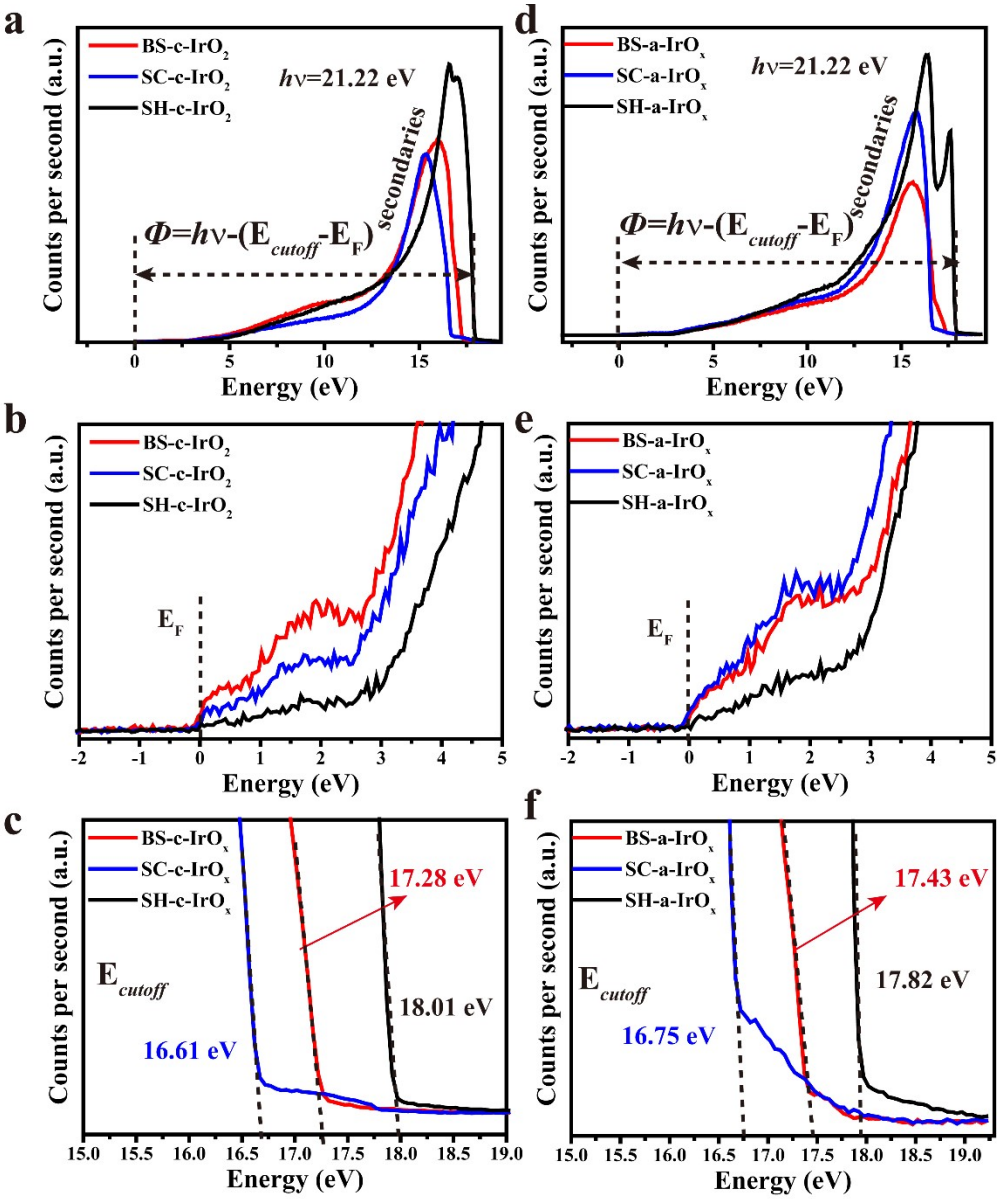

Figure S8. The work function of prepared IrOx NPs measured using UPS. (a) and (d) are the full spectra of crystalline and amorphous, respectively. (b) and (e) are Fermi level zone of UPS spectra, all of them have intensity in the region, so it can be assumed that $E_F = 0$. (c) and (f) fitting the cut-off edge of the UPS spectra of secondary electrons to obtain E_{cutoff}.

Table S3. The calculated Φ according to the UPS spectra**.**

Catalyst	E_F	E_{cutoff} (eV)	Φ (eV)
SH-c-IrO_x	0	18.01	3.21
SC-c-IrO_x	0	17.28	4.61
BS-c-IrO_x	0	16.61	3.94
SH-a-IrO_x	0	17.82	3.4
SC-a-IrO_x	0	16.75	4.47
BS-a-IrO_x	0	17.43	3.79

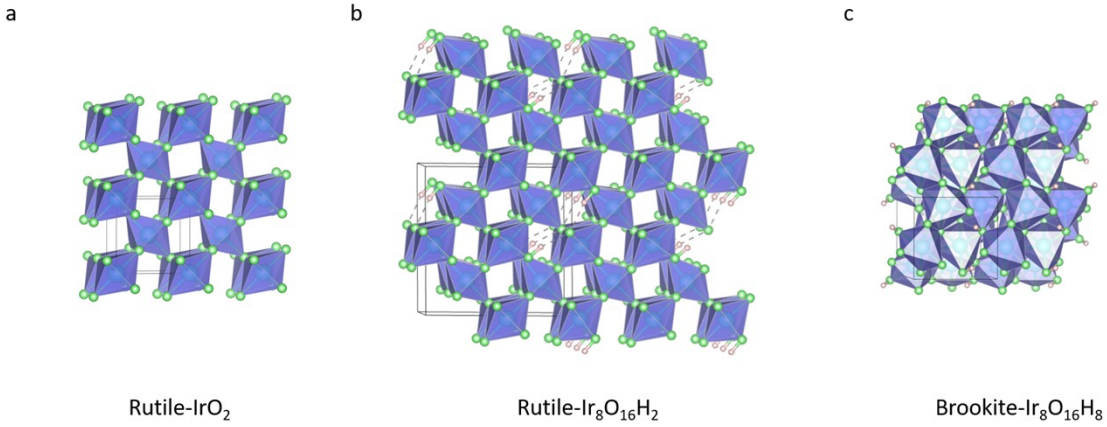

Figure S9. (a). The optimized rutile IrO_2 structure diagram. (b). The optimized 2×2 rutile $Ir_8O_{16}H_2$ structure constructed basing on the rutile IrO_2. (c). The optimized Brookite $Ir_8O_{16}H_8$ structure diagram.

Note: DFT calculation was conducted to explore the origin of the high OER activity of BS-IrO_x. As we know, it is often tricky to simulate amorphous structures. The amorphous structure is always accompanied by abundant defect sites and plenty of hydroxyl groups inside, which is different from the traditional crystal surface structure. In order to approximate the construction of the iridium-based amorphous structure model, the following factors are considered in this work: the surface hydroxyl groups, the valence state of iridium, and the connection mode between [IrO_n]-[IrO_n] (the ratio of the edge-shared and the corner-shared). According to work conducted by Mavračic et al.[2], amorphized rutile oxides have the higher proportion of edge-shared [MO_n]-[MO_n] unit versus the pristine rutile oxide. The connecting structure of brookite and its average M-O bond length is highly similar to the amorphous structure. Additionally, the higher proportion edge-shared connection mode in the interfacial amorphous sample was also confirmed by Yang et al.[3] Therefore, in the construction of amorphous oxides in this work, we adopt the brookite-TiO_2 serving as the model frame, the Ir atoms replaced the Ti atoms. The OH species driving from the XPS results were constructed by filling the geometric vacancy in Ir-brookite.

Table S4. The calculated Fermi level of constructed IrO_2.

Catalysts	IrO_2-c-R	IrO_2-a-R	IrO_2-a-B
E_F (eV)	**-0.254**	**-0.874**	**-1.079**

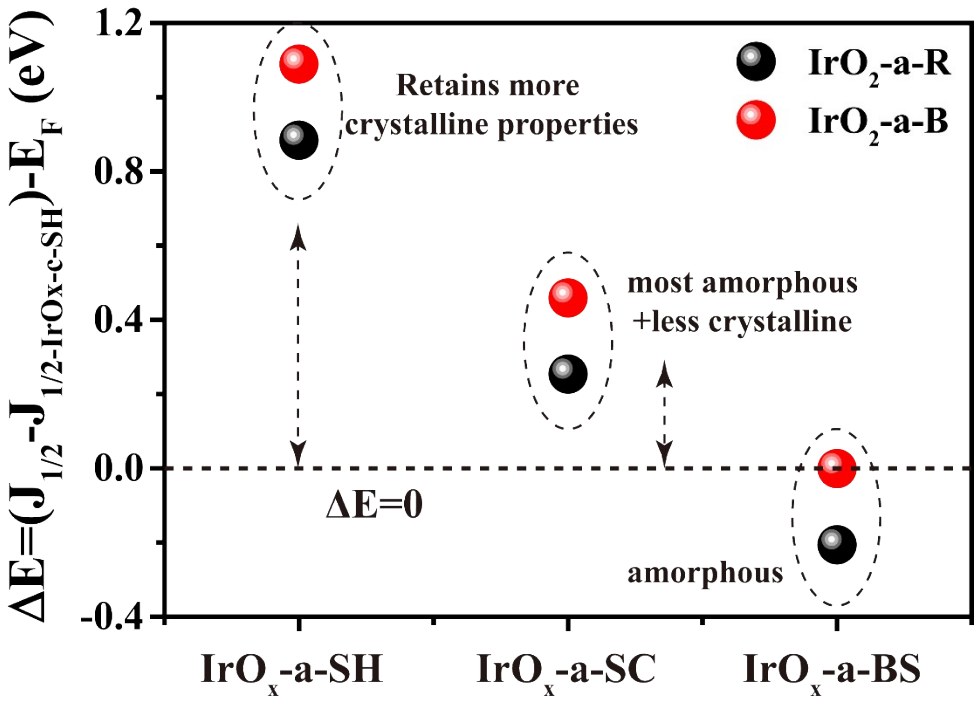

Figure S10. Verification of model credibility by Fermi energy levels difference. Since the Fermi energy level is basically across the t_{2g} band, thus the energy of $J_{1/2}$ can be used as a reference for the Fermi energy level. Here, we use $J_{1/2}$ of SH-c-IrO_x as a benchmark, because the IrO_x prepared in NaOH medium is widely used and is also more realistic. For IrO_2-a-R, the $\Delta E=(J_{1/2}-J_{1/2\text{-}IrOx\text{-}c\text{-}SH})-E_F$(=-0.874) and the ΔE of IrO_2-a-B are calculated by $(J_{1/2}-J_{1/2\text{-}IrOx\text{-}c\text{-}SH})-E_F$(=-1.079). The large value of ΔE means the material retains more crystalline properties, while the small value of ΔE means the material has part of amorphous. If the ΔE=0, then the model matches well with the properties of the prepared material.

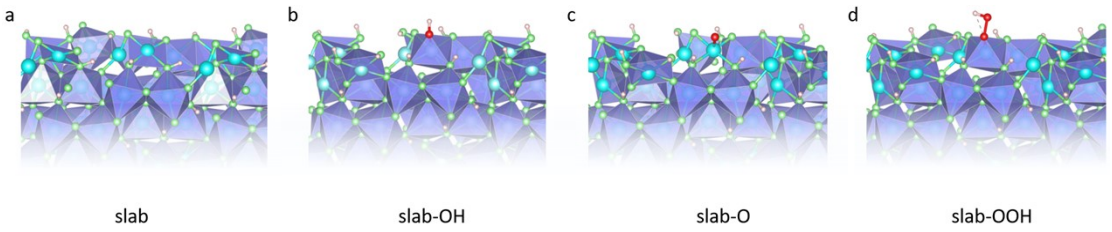

Figure S11. (a)~(d). The optimized surface adsorption model of Brookite-Ir.

Note: The [210] surface was cleaved from the relaxed bulk Ir-brookite serving as the adsorbed surface as it was the thermodynamically stable. Four layers thickness with below two-layer fixed and top two-layers relaxed. A vacuum region of 15 Å was adopted in this work. According to the results of relaxed slab mode, the Iridium atom in a low coordination environment was selected as the adsorbed site. As shown in the Figure, the adsorbed models were present. Herein, the previous work has demonstrated that the O*-O* directly coupling process in lattice oxygen participation mechanism (LOM) is less favorable to the amorphous structure.[4] Therefore, the adsorbed oxygen mechanism (AEM) was considered in this work.

Figure S7-Figure S8 References:

1. Sun, W.; Song, Y.; Gong, X. Q.; Cao, L. M.; Yang, J., An efficiently tuned d-orbital occupation of IrO_2 by doping with Cu for enhancing the oxygen evolution reaction activity. *Chem Sci* **2015,** *6* (8), 4993-4999.

2. Mavračić, J.; Mocanu, F. C.; Deringer, V. L.; Csányi, G.; Elliott, S. R., Similarity Between Amorphous and Crystalline Phases: The Case of TiO2. *The Journal of Physical Chemistry Letters* **2018,** *9* (11), 2985-2990.

3. May, K. J.; Carlton, C. E.; Stoerzinger, K. A.; Risch, M.; Suntivich, J.; Lee, Y.-L.; Grimaud, A.; Shao-Horn, Y., Influence of Oxygen Evolution during Water Oxidation on the Surface of Perovskite Oxide Catalysts. *The Journal of Physical Chemistry Letters* **2012,** *3* (22), 3264-3270.

4. Gao, J.; Xu, C. Q.; Hung, S. F.; Liu, W.; Cai, W.; Zeng, Z.; Jia, C.; Chen, H. M.; Xiao, H.; Li, J.; Huang, Y.; Liu, B., Breaking Long-Range Order in Iridium Oxide by Alkali Ion for Efficient Water Oxidation. *J Am Chem Soc* **2019,** *141* (7), 3014-3023.

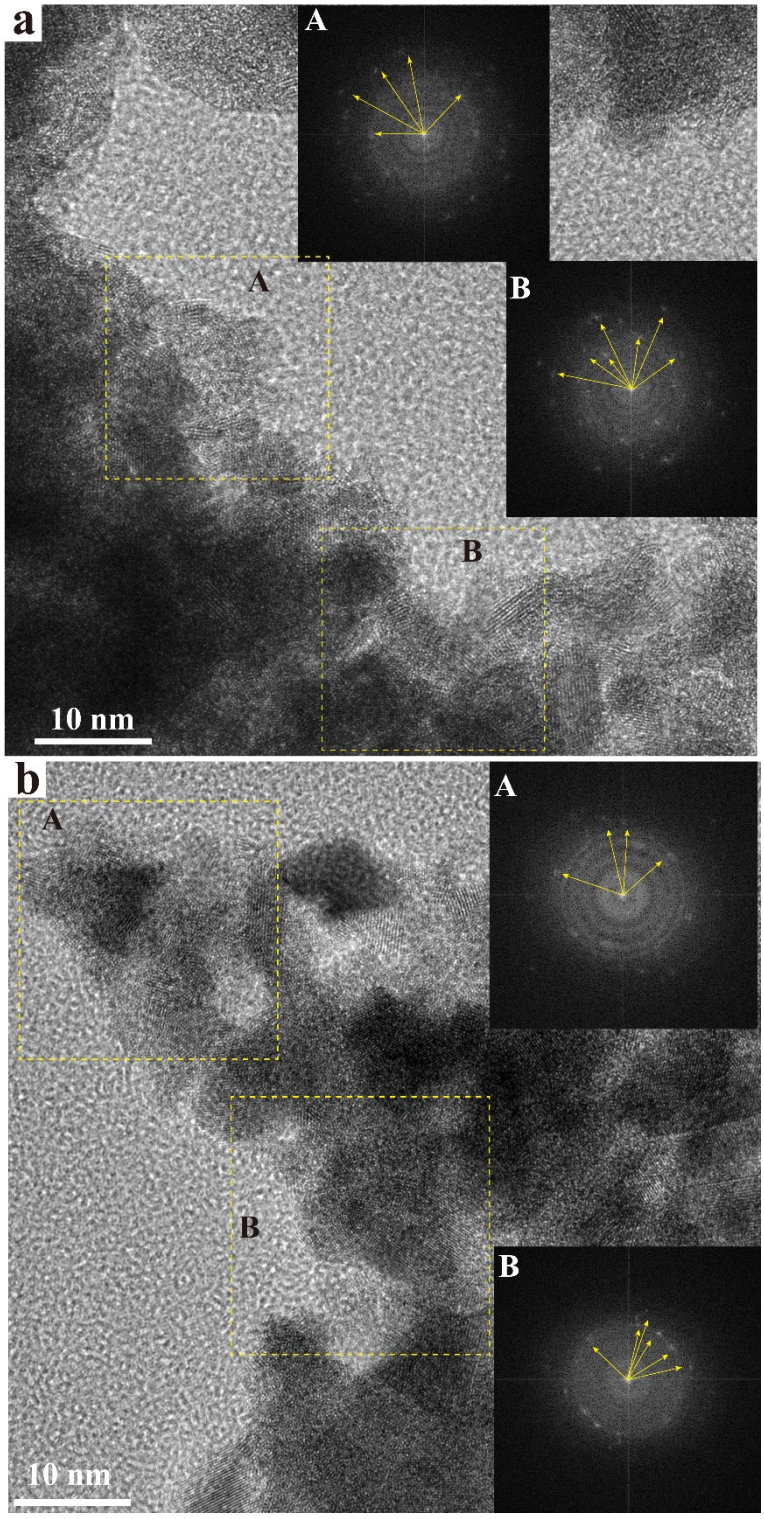

Figure S12. HRTEM images and matrix SAED patterns of prepared BS-a-IrO_x. The pseudo-crystalline morphology of BS-a-IrO_x are widely distributed. As displayed in SAED patterns, in addition to the amorphous rings there are also scattered weak dotted structures indicating the formation of weak crystalline facets, which exist only in a very short range as the selected matrix area is quite small, and these facets are mainly (200) and (220) rather than the common (110) and (101) facets of the crystalline structure.

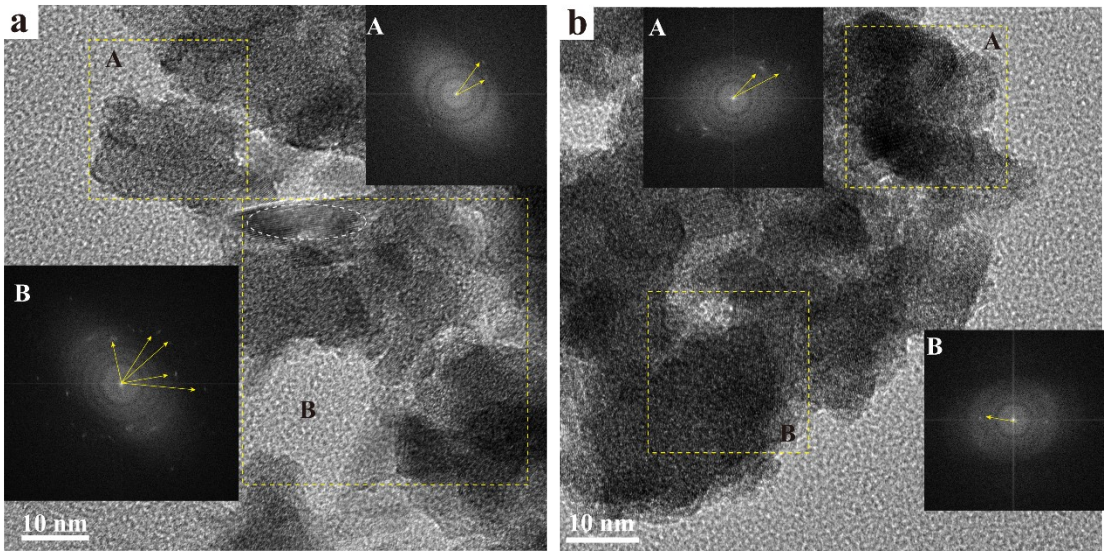

Figure S13. HRTEM images and matrix SAED patterns of prepared SC-a-IrO_x. The pseudo-crystalline morphology of SC-a-IrO_x are much less compared to BS-a-IrO_x. According to the SAED calculations it is clear that these small number of dots also correspond to the (200) and (220) faces, but we also find an extremely small number of crystalline structures (the white dashed ellipse in Figure a).

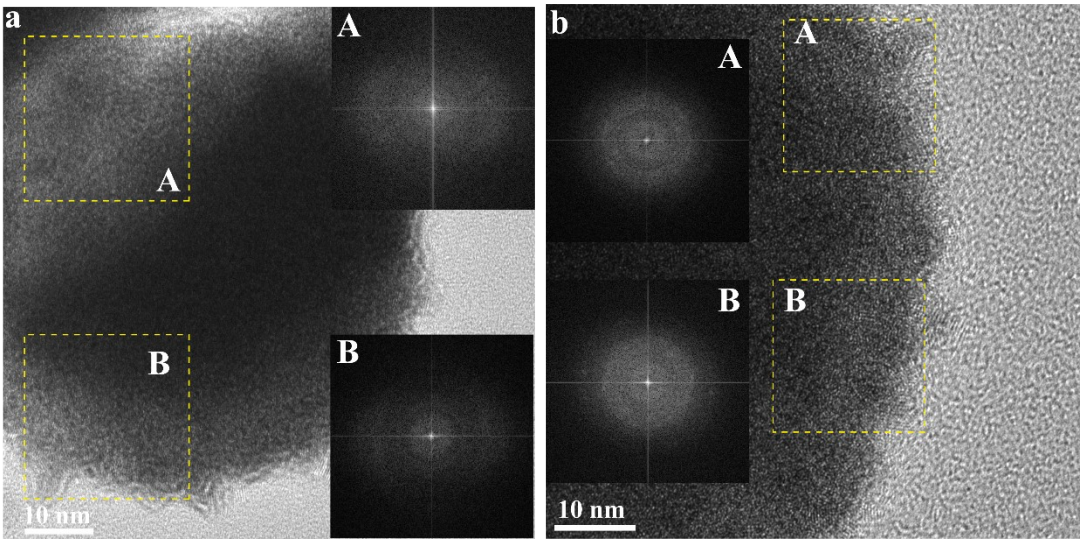

Figure S14. HRTEM images and matrix SAED patterns of prepared SH-a-IrO_x. The pseudo-crystalline morphology of SH-a-IrO_x are very rare.

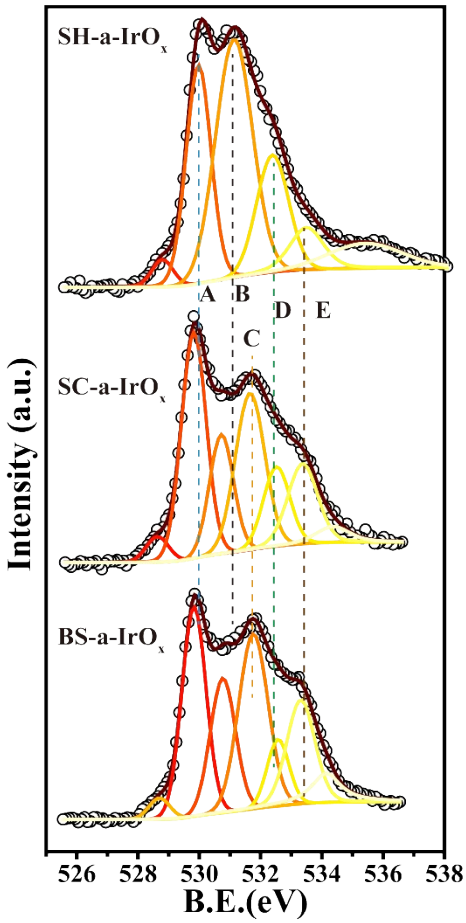

Catalysts	A (Ir-O)		B (Ir-OH)		C (-COH)		D (H_2O)		E (C-O)	
	B.E. (eV)	Area ratio	B.E. (eV)	Area ratio	B.E. (eV)	Area ratio	B.E. (eV)	Area ratio	B.E. (eV)	Area ratio
SH-a-IrO$_x$	530.0	0.25	531.1	0.40	\	\	532.4	0.17	533.5	0.07
SC-a-IrO$_x$	529.8	0.32	530.7	0.15	531.7	0.22	532.5	0.11	533.4	0.13
BS-a-IrO$_x$	529.8	0.28	530.8	0.17	531.8	0.26	532.6	0.07	533.3	0.17

Figure S15. The performed O-1s XPS spectra of amorphous IrO_x NPs. All the spectra are calibrated by C-1s at the binding energy of 284.8 eV. The deconvoluted results are listed below.

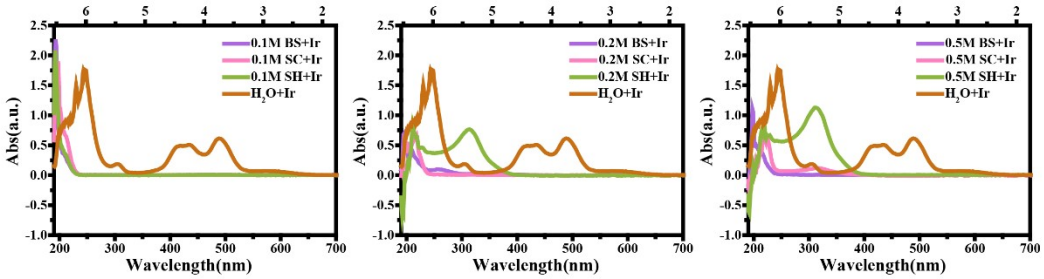

Figure S16. UV-Vis spectra of the Ir ions residues in three alkaline medium filtrates with different concentrations after hydrothermal reaction. At low concentrations, all three media showed good conversions as there were no peaks associated with Ir in the UV-VIs range, but when the concentration was increased to 0.2 M, significant peaks appeared in the UV region especially for SC and SH, and the peak at 335 nm (from $[Ir(OH)_4^{2-}]$) for SH was unusually strong. As the concentration was increased to 0.5 M, there were residues in all three media, but SH was more obvious, and the actual measured yields also verified this phenomenon, because there was almost no solid formation at 0.5 M SH.

Table S5. The yields of prepared IrO_x by selected three sodium bases with different concentrations.

	Medium solution		**H_2IrCl_6 solution (20mg ml^{-1})**		**Amorphous[a]**		**Crystalline[b]**	
	Concentration /mol L^{-1}	Volume /ml	Volume /ml	IrO_2 Theoretical weight/mg	Actual weight/mg	Yield (%)[c]	Actual weight/mg	Yield (%)
BS-IrO_x	0.05	20	4	34.8	37.7	108.3	35.1	100.8
	0.1	20	4	34.8	37.4	107.5	35.4	101.7
	0.5	20	4	34.8	36.1	103.7	35	100.6
SC-IrO_x	0.05	20	4	34.8	35.6	102.3	34.7	99.7
	0.1	20	4	34.8	37.3	107.2	34.8	100.0
	0.5	20	4	34.8	29.2	83.9	20.2	58.0
SH-IrO_x	0.05	20	4	34.8	33.2	98.3	32.1	92.2
	0.1	20	4	34.8	32.4	93.1	30	86.2
	0.5	20	4	34.8	2.6	7.5	<1.5	<4

Notes: [a]- The powder obtained after filtration were dried at 50 °C for 30 min and then transferred to a furnace for calcination at 350 °C for 6h;

[b]- The powder obtained after filtration were dried at 50 °C for 30 min and then transferred to a furnace for calcination at 400 °C for 12 h;

[c]- The yield can be greater than 100% due to a small amount of water and adsorbed impurities that are not completely removed, so greater than 100% we consider it as 100%. It is also important to note that some powder remains on the filter paper.

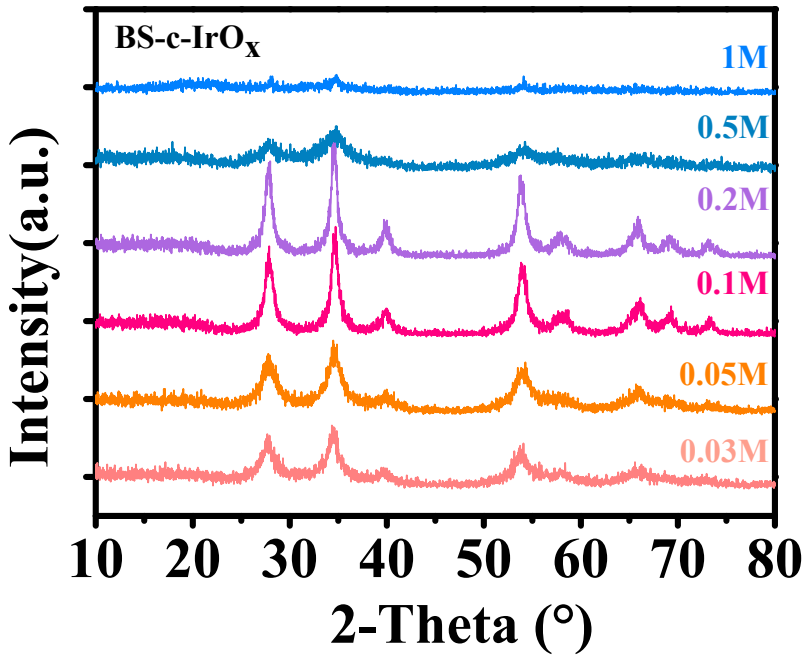

Figure S17. XRD patterns of the IrO_x synthesized at a series of concentrations BS under calcination conditions of 400 °C for 12 h.

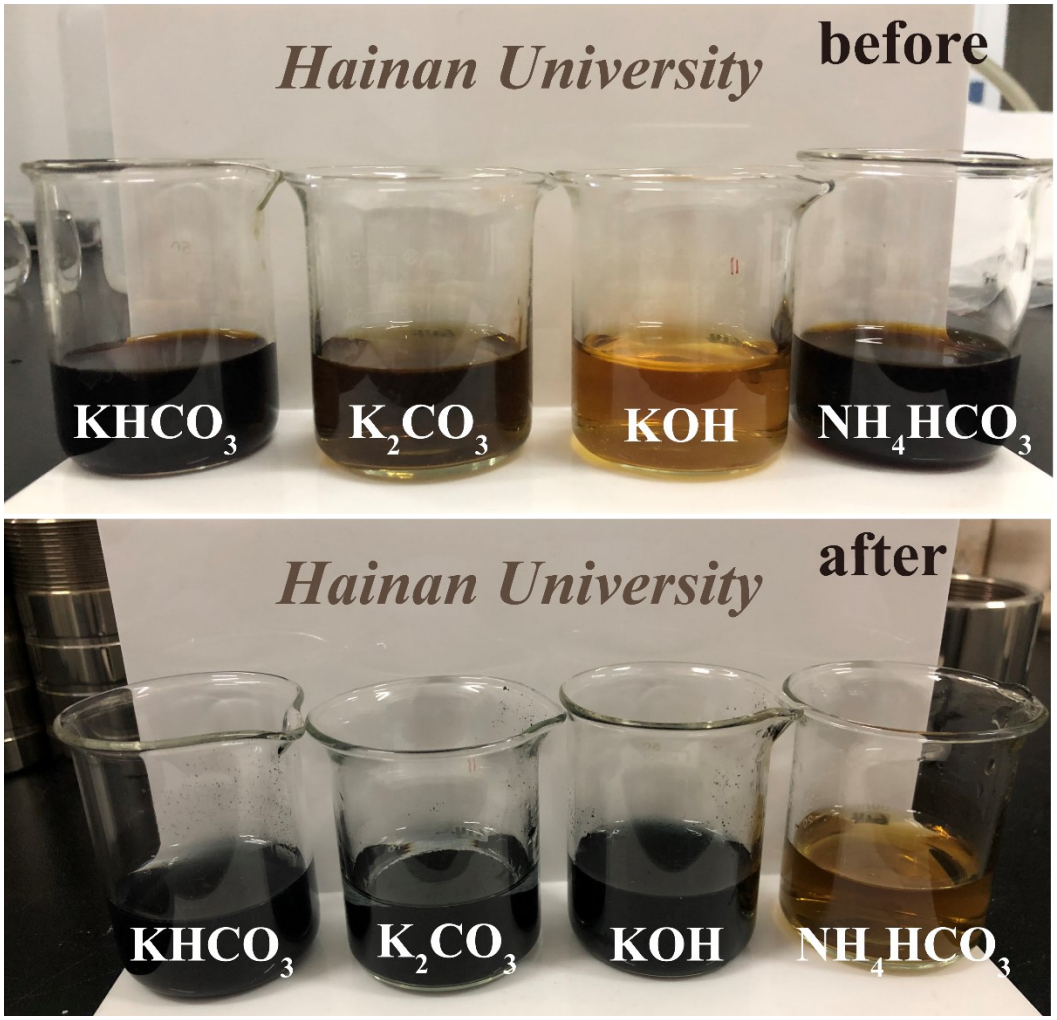

Figure S18. Photographs before and after synthesis of IrO_x in different media. The selected three potassium bases have a large amount of solid formation after hydrothermal treatment, but NH_4HCO_3 remains a clear solution.

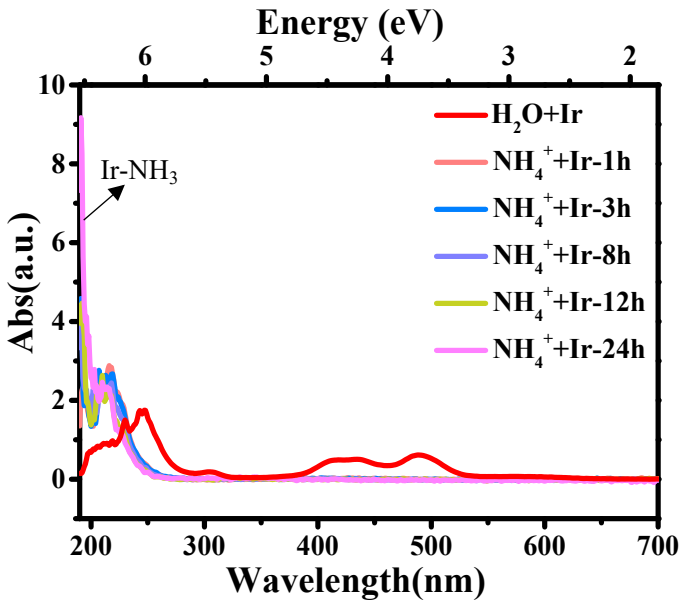

Figure S19. UV-Vis spectra recorded nucleation differences of $IrCl_6^{2-}$ under the NH_4HCO_3 solution. Strong absorption peaks appear in the UV region and become increasingly strong with time, which may closely relate to the formation of a new coordination between Ir and NH_3.